Functional impact of pathogenic Runt domain mutations in *Runx2 in vivo*: Insights into the skeletal and dental anomalies of cleidocranial dysplasia

Saki Ogawa[1,2,*], Shinnosuke Higuchi[1,*], Yuki Yoshimoto[1,*, §], Mari Hoshino[1,3], Shigenori Miura[1], Atsuko Hamada[3], Hitomi Watanabe[4], Tetsushi Sakuma[5], Kadi Hu[1], Shun Ogata[1,2], Kenta Uchibe[6], Katsumi Fujimoto[1], Takashi Yamamoto[7], Tetsuji Okamoto[3], Ryo Kunimatsu[2], Yusuke Sotomaru[8], Kotaro Tanimoto[2], Gen Kondoh[4], Denitsa Docheva[9], and Chisa Shukunami[1]†

[1]Department of Molecular Biology and Biochemistry, Graduate School of Biomedical & Health Sciences, Hiroshima University, Hiroshima 734-8553, Japan

[2]Department of Orthodontics and Craniofacial Developmental Biology, Graduate School of Biomedical and Health Sciences, Hiroshima University, Hiroshima 734-8553, Japan

[3]Department of Oral Oncology, Graduate School of Biomedical & Health Sciences, Hiroshima University, Hiroshima 734-8553, Japan

[4]Laboratory of Integrative Biological Science, Institute for Life and Medical Sciences, Kyoto University, Kyoto 606-8507, Japan

[5]Graduate School of Agriculture, Kyoto University, Kyoto 606-8502, Japan

[6]Department of Maxillofacial Anatomy and Neuroscience, Graduate School of Biomedical & Health Sciences, Hiroshima University, Hiroshima 734-8553, Japan

[7]Division of Integrated Sciences for Life, Graduate School of Integrated Sciences for Life, Hiroshima University, Higashi-Hiroshima, Hiroshima 739-8526, Japan

[8]Natural Science Center for Basic Research and Development, Hiroshima University, Hiroshima 734-8553, Japan

[9]Department of Musculoskeletal Tissue Regeneration, Orthopaedic Hospital König-Ludwig-Haus, Julius-Maximilians-University Würzburg, 97074 Würzburg, Germany

[§]**Present address:** Department of Molecular Craniofacial Embryology and Oral Histology, Graduate School of Medical and Dental Sciences, Institute of Science Tokyo, Tokyo 113-8510, Japan

Running title: CCD mouse model with pathogenic Runx2 mutations

Key words: *Runx2*; Cleidocranial dysplasia; Runt domain; skeletogenesis; tooth root furcation.

*These authors contributed equally to this work.

†Address all correspondence to Chisa Shukunami, DDS, Ph.D.
Department of Molecular Biology and Biochemistry, Graduate School of Biomedical & Health Sciences, Hiroshima University, Hiroshima 734-8553, Japan
Tel: +81-82-257-5628
shukunam@hiroshima-u.ac.jp

ABSTRACT

Runt-related transcription factor 2 (RUNX2) is a key transcription factor for skeletogenesis, and mutations in its gene cause cleidocranial dysplasia (CCD), an autosomal dominant skeletal disorder. The evolutionarily conserved 128-amino acid Runt homology domain (RHD) of human RUNX2 is essential for DNA binding and heterodimerization, and serves as a mutation hotspot associated with severe CCD phenotypes. To elucidate the functional impact of pathogenic RHD mutations *in vivo*, we generated two novel mouse lines: one carrying a missense mutation, c.695G>A (p.R232Q) (*Runx2*$^{m/+}$), corresponding to the human *RUNX2* c.674G>A (p.R225Q), and the other harboring a frameshift mutation, c.697_698delGA (p.E233TfsTer9) (*Runx2*$^{\Delta 2/+}$), causing a premature stop codon. Homozygous *Runx2*$^{m/m}$ and *Runx2*$^{\Delta 2/\Delta 2}$ mice exhibited a complete loss of membranous ossification, whereas heterozygous *Runx2*$^{m/+}$ and *Runx2*$^{\Delta 2/+}$ mice displayed typical CCD-like skeletal features, including an open anterior fontanelle and clavicle hypoplasia. Unexpectedly, heterozygotes carrying pathogenic mutations in RHD developed an accessory root-like protrusion at the furcation of three-rooted maxillary first molars, representing a previously unrecognized dental phenotype during root development. Dual luciferase assays revealed impaired transactivation of the p.R232Q mutant Runx2 on the osteocalcin enhancer/promoter. Wild-type Runx2 was robustly expressed in osteoblasts and hypertrophic chondrocytes during bone formation, but the mutant Runx2 exhibited reduced expression in hypertrophic chondrocytes and partially impaired nuclear localization, resulting in arrested osteoblast and chondrocyte maturation. Our mutant mouse model provides a valuable *in vivo* platform to study CCD pathogenesis, mechanisms of tooth root furcation, and therapeutic interventions targeting dysfunctional RHD.

67 **INTRODUCTION**

68 Cleidocranial dysplasia (CCD; OMIM #119600) is a rare autosomal dominant skeletal and
69 dental disorder caused by haploinsufficiency of the *Runt-related transcription factor 2*
70 (*RUNX2*)[1,2]. CCD affects one in a million people worldwide, with no gender or ethnic
71 differences, although mild cases may be underdiagnosed[3]. Clinical features include clavicular
72 hypoplasia or aplasia, midfacial hypoplasia, delayed closure of cranial sutures, Wormian bones,
73 and a persistent anterior fontanelle closure, often with short stature and dental anomalies[1].
74 Prolonged retention of deciduous teeth and multiple unerupted supernumerary permanent teeth
75 are frequently encountered in dental clinics[3-5], requiring long-term multidisciplinary care,
76 including oral and maxillofacial surgery and orthodontics, to manage function, aesthetics, and
77 patient burden.

78 The human *RUNX2* and mouse *Runx2* genes comprise 8 exons, spanning approximately 218
79 kb (hg38, NM_001024630.4) and 206 kb. (mm39, NM001271627.2), respectively[6,7].
80 Homozygous *Runx2*-deficient mice die shortly after birth from respiratory failure, exhibiting a
81 complete lack of ossification and arrested embryonic tooth development, while heterozygous
82 mice exhibit persistent open anterior fontanelle, clavicle hypoplasia, and other skeletal
83 abnormalities resembling human CCD[2,8]. RUNX2/Runx2 is a key transcription factor in
84 skeletal development, regulating mesenchymal commitment to the osteoblastic lineage,
85 chondrocyte and osteoblast proliferation, chondrocyte maturation, and transdifferentiation of
86 hypertrophic chondrocytes into osteoblasts[9,10]. Intramembranous ossification strongly depends
87 on *Runx2* and requires higher levels of its expression compared to endochondral ossification[6].
88 In *Runx2*$^{+/-}$ mice, as in human CCD, delayed eruption of incisors and maxillary first molars
89 occurs due to impaired osteoclast recruitment in the alveolar bone, although neither impacted
90 nor supernumerary teeth are present[11].

91 RUNX2 contains several functional domains, including a glutamine alanine-rich domain
92 (QA), a highly conserved Runt homology domain (RHD), a proline serine threonine domain
93 (PST), and a C-terminal VWRPY motif, and harbors a nuclear transition signal (NLS) at the C-
94 terminus of the RHD and a nuclear matrix targeting signal (NMTS)[12]. More than 200 *RUNX2*
95 mutations have been reported in CCD patients, including frameshift, missense, nonsense, and
96 splice-site variants[7,13]. While nonsense and frameshift mutations are distributed throughout the
97 gene, most missense mutations cluster within the 128-amino acid RHD, which is critical for
98 DNA binding and heterodimerization with core-binding factor subunit β (Cbfb)[7,14,15]. Many
99 pathogenic mutations associated with CCD, especially those linked to severe dental anomalies,
100 are missense or nonsense mutations affecting the RHD[7]. However, the mechanisms by which
101 these mutations cause severe CCD have long remained unclear, owing to the absence of *in vivo*
102 models with RHD-specific mutations and the limitations of cellular systems that cannot fully
103 recapitulate the disease complexity.
104 Recently, several disease-specific induced pluripotent stem (iPS) cell lines carrying
105 mutations such as p.R225Q, p.S124W, p.R391X, and p.Q67X have been established from
106 patients[16-18]. iPS cells harboring nonsense mutations p.Q67X in the QA domain and p.R391X
107 in the NTMS domain exhibit reduced osteogenic differentiation capacity[16]. Transplantation of
108 osteoblasts induced from p.Q67X iPS cells into rat calvarial defects led to limited bone
109 regeneration, which was rescued by genetic correction of the *RUNX2* mutation[16]. While
110 disease-specific iPS cells are useful for modeling altered differentiation potential and cellular
111 behavior *in vitro* but fail to recapitulate morphogenetic processes during development.
112 Furthermore, iPS cells from CCD patients with heterozygous *RUNX2* mutations do not allow
113 comprehensive evaluation of mutant protein function. Despite extensive studies on RUNX2
114 and CCD, the *in vivo* impact of RHD mutations is still not well characterized.

115 In this study, we generated two novel mouse models carrying RHD mutations: a missense
116 mutation (c.695G>A; p.R232Q) and a frameshift mutation (c.697_698delGA; p.E233TfsTer9).
117 These models serve as a robust platform for investigating CCD pathogenesis and uncover
118 previously unrecognized abnormalities in tooth root furcation. By enabling detailed functional
119 analysis of RHD mutations in a disease-relevant context, they provide new insights into CCD
120 pathogenesis and may contribute to the development of targeted therapies.
121

122 **RESULTS**

123 Establishment of CCD mouse models harboring *Runx2* missense or frameshift mutations

124 The mouse *Runx2* gene, located on chromosome 17 and composed of 8 exons, is transcribed
125 from two distinct promoters: distal P1 and proximal P2, generating isoforms with different N-
126 terminal amino acid sequences[7] (Fig. 1a, Fig. S1a). The 128-amino-acid RHD crucial for DNA
127 binding, is encoded by exons 2 to 4, and the NLS by exons 4 and 5 (Fig. 1b). CCD patients with
128 a heterozygous p.R225Q mutation in human *RUNX2* show multiple supernumerary teeth and
129 membranous bone dysplasia[17,19-21]. In mouse *Runx2*, this mutation corresponds to p.R232Q
130 owing to seven additional amino acids at the N-terminus. We introduced the c.695G>A
131 (p.R232Q) mutation into the RHD of *Runx2*. To introduce the mutation via homology-directed
132 repair (HDR), we used Platinum TALENs and a single-stranded oligodeoxynucleotide (ssODN)
133 containing the c.695G>A substitution and a silent ApaI site for genotyping (Fig. 1a).
134 Microinjection of Platinum TALEN mRNAs and a designed ssODN into fertilized eggs
135 generated 51 mice, including 14 with non-homologous end joining induced indels and 2 carried
136 the HDR-mediated knock-in allele (Table S1). Lines carrying the missense (*m*) or the double-
137 nucleotide deletion (*Δ2*) mutation were established from founder mice (Fig. 1c, Fig. S1a, b). In
138 *Δ2* mutants, deletion of nucleotides 697G and 698A caused a frameshift mutation, generating a

139 premature stop codon at 241 (Fig. S1b, Fig. 1c). For genotyping, SmaI digestion yielded 115
140 bp and 80 bp fragments for the wild-type allele, while mutant alleles produced an undigested
141 195 bp fragment, and ApaI digestion generated 113 bp and 82 bp fragments specific to the
142 missense mutant allele (Fig. S2). Direct sequencing confirmed that *Runx2*$^{m/+}$ carried both the
143 c.690T>G silent andc.695G>A missense mutations, while *Runx2*$^{\Delta 2/+}$ harbored a two-nucleotide
144 deletion causing a premature stop codon. (Fig. 1d). Thus, we successfully established two
145 distinct CCD model mice: one with a clinically relevant RHD missense mutation associated
146 with severe CCD and another with a frameshift mutation.
147
148 Defective bone formation in homologous *Runx2* RHD-mutant mice
149 At embryonic day 18.5 (E18.5), *Runx2*$^{+/+}$, *Runx2*$^{m/+}$, and *Runx2*$^{\Delta 2/+}$ embryos were similar in
150 size and morphology, while *Runx2*$^{m/m}$ and *Runx2*$^{\Delta 2/\Delta 2}$ embryos were smaller with limb
151 shortening, facial underdevelopment, and calvarial defects (Fig. S3a-e). Skeletal development
152 at E18.5 was compared among wild-type, heterozygous, and homozygous *Runx2* RHD mutants
153 (Fig. 2a-j). In *Runx2*$^{+/+}$ embryos, intramembranous ossification progressed in the calvaria and
154 clavicles, and endochondral ossification in the axial and appendicular skeletons (Fig. 2a, f, g).
155 In *Runx2*$^{m/+}$ or *Runx2*$^{\Delta 2/+}$ embryos, intramembranous ossification occurred but was impaired,
156 causing clavicle hypoplasia and delayed fontanelle closure (Fig. 2b, c, h, i). In *Runx2*$^{m/m}$ or
157 *Runx2*$^{\Delta 2/\Delta 2}$ embryos, intramembranous ossification was absent, causing skull and clavicle
158 defects, and endochondral ossification was impaired, with long bones remaining mostly
159 cartilaginous and mineralization limited to the forearms and the lower legs (Fig. 2d, e, j).
160 Forelimb calcification was more delayed in *Runx2*$^{m/m}$ than in *Runx2*$^{\Delta 2/\Delta 2}$ embryos (Fig. 2d, e).
161 Histological sections of the forearm from *Runx2*$^{+/+}$, *Runx2*$^{m/+}$, *Runx2*$^{m/m}$ and *Runx2*$^{\Delta 2/\Delta 2}$
162 embryos at E18.5 were stained with toluidine blue (TB), alkaline phosphatase (ALP), and

163 Alizarin Red (AR) (Fig. 3a-c). In *Runx2*$^{+/+}$ and *Runx2*$^{m/+}$ embryos, primary ossification canters
164 formed in the diaphysis, with metachromatic cartilage present in the metaphysis and epiphysis.
165 In *Runx2*$^{m/m}$ and *Runx2*$^{\Delta 2/\Delta 2}$ embryos, the entire bone primordium consisted exclusively of
166 cartilage (Fig. 3a). ALP activity was high from the diaphysis to the metaphysis in *Runx2*$^{+/+}$ and
167 *Runx2*$^{m/+}$ embryos, but was restricted to the hypertrophic/calcified cartilage in the center of the
168 ulna and radius of *Runx2*$^{m/m}$ and *Runx2*$^{\Delta 2/\Delta 2}$ embryos (Fig. 3b). Although the calcified area was
169 smaller than the ALP^{+} area in all genotypes, in *Runx2*$^{m/m}$ and *Runx2*$^{\Delta 2/\Delta 2}$ embryos, both regions
170 were markedly smaller than those in *Runx2*$^{+/+}$ and *Runx2*$^{m/+}$ embryos and were confined to the
171 central diaphysis where hypertrophic chondrocytes were present (Fig. 3c). Notably, calcified
172 cartilage was smaller in *Runx2*$^{m/m}$ than in *Runx2*$^{\Delta 2/\Delta 2}$ embryos, suggesting delayed cartilage
173 maturation (Fig. 3a-c).

174 To assess chondrogenic and osteogenic marker expression, the forearm of *Runx2*$^{+/+}$,
175 *Runx2*$^{m/+}$ and *Runx2*$^{m/m}$ embryos at E18.5 were analyzed by *in situ* hybridization (Fig. 3d-j).
176 Early chondrogenic markers *Col2a1* and *Acan* were expressed in proliferating and mature
177 chondrocytes in *Runx2*$^{+/+}$, *Runx2*$^{m/+,}$ and *Runx2*$^{m/m}$ embryos (Fig. 3d, e). *Ihh* was expressed in
178 prehypertrophic chondrocytes in *Runx2*$^{+/+}$ and *Runx2*$^{m/+}$ embryos, whereas its expression was
179 only faintly detected in the central diaphysis of *Runx2*$^{m/m}$ embryos (Fig. 3f). *Col10a1* was
180 expressed in hypertrophic chondrocytes of the metaphysis in *Runx2*$^{+/+}$ and *Runx2*$^{m/+}$ embryos,
181 but only weakly detected in hypertrophic chondrocytes in the central diaphysis in *Runx2*$^{m/m}$
182 embryos (Fig. 3g). In *Runx2*$^{+/+}$ and *Runx2*$^{m/+}$ embryos, *Runx2* and *Spp1* were expressed in
183 osteoblasts, osteocytes, and chondrocytes (Fig. 3h, i). In *Runx2*$^{m/m}$ embryos, *Runx2* was faintly
184 expressed in chondrocytes and perichondrial cells, while *Spp1* was detected in a small
185 population of hypertrophic chondrocytes in the diaphysis (Fig. 3h, i). *Col1a1* was detected in
186 osteoblasts, osteocytes, cells of the periosteum and perichondrium in *Runx2*$^{+/+}$ and *Runx2*$^{m/+}$

187 embryos, but only faintly in the perichondrium of *Runx2*$^{m/m}$ embryos (Fig. 3j).

188 These findings demonstrate that RHD mutations disrupt both intramembranous and
189 endochondral ossification, emphasizing the essential role of the RHD in skeletal development.

190

191 Functional impairment of Runx2 caused by the p.R232Q mutation in the RHD

192 Wild-type and p.R232Q mutant Runx2 proteins were analyzed by Western blotting using
193 whole-cell extracts from HEK293T cells transfected with each construct (Fig. 4a).
194 Immunoblotting with an anti-RUNX2 antibody recognizing a peptide around Arg (R) at 267 of
195 human RUNX2 confirmed the expression of both wild-type and mutant Runx2, with no
196 apparent differences, although a sight size shift was observed due to the FLAG tag (Fig. 4a, Fig.
197 S4a). Next, Western blotting with the same anti-RUNX2 antibody was performed on forelimb
198 extracts from *Runx2*$^{+/+}$, *Runx2*$^{m/+}$, and *Runx2*$^{m/m}$ embryos at E18.5 to assess Runx2 expression
199 (Fig. 4b, Fig. S4b). The reported molecular weights are approximately 57 kDa for isoform 1
200 (MASNS) and 56 kDa for isoform 2 (MRIPV)[22]. Both wild-type and p.R232Q mutant Runx2
201 showed similar sizes in HEK293T whole-cell extracts transfected with each construct (Fig. 4a,
202 Fig. S4a) and in tissue extracts from *Runx2*$^{+/+}$, *Runx2*$^{m/+}$ and *Runx2*$^{m/m}$ embryos, although the
203 expression level was markedly reduced in *Runx2*$^{m/m}$ embryos compared to *Runx2*$^{+/+}$ embryos
204 (Fig 4b, Fig. S4b).

205 The *p6OSE2-luc* vector contains six tandem repeats of osteoblast-specific element 2 (OSE2,
206 AACCACA) from the mouse osteocalcin promoter, a Runx2 binding site, followed by a
207 minimal promoter driving firefly luciferase expression, allowing quantification of Runx2-
208 dependent transcription[23,24]. To evaluate the effect of RHD mutations, HEK293T cells were
209 transfected with wild-type or mutant Runx2 (p.R232Q, p.R232W, or p.R200X) (Table S2),
210 along with *p6OSE2-luc* and the *pGL4.74[hRlux/TK]* internal control, and dual luciferase assays

211 were performed (Fig. 4c). Wild-type Runx2 showed a 6.7-fold increase in transcriptional
212 activity compared to the empty vector, whereas the p.R232Q, p.R232W, or p.R200X mutants
213 exhibited activity comparable to the empty vector, indicating that missense and nonsense
214 mutations in the RHD abolish Runx2-mediated activation via OSE2 (Fig. 4c).

215 The p.R232Q mutation lies near the NLS in the C-terminal region of the RHD[25], potentially
216 affecting Runx2 nuclear translocation. To examine the impact of the mutation on intracellular
217 localizations, immunostaining was performed on sections of the ulna sections from *Runx2*$^{+/+}$
218 and *Runx2*$^{m/m}$ embryo at E18.5 using anti-Col10 and anti-Runx2 antibodies (Fig. 5a-d).
219 Consistent with the results of *in situ* hybridization (Fig. 3g, h), In *Runx2*$^{+/+}$ embryos, Col10
220 accumulated abundantly in the metaphysis and in cartilage remnants of the primary spongiosa
221 (Fig. 5a), while Runx2^{+} cells were distributed from the metaphysis to the diaphysis (Fig. 5b).
222 In *Runx2*$^{m/m}$ mice, Col10^{+} hypertrophic chondrocytes were confined to the central diaphysis
223 (Fig. 5c), and Runx2^{+} cells were more widely distributed but with markedly weaker signal
224 intensity (Fig. 5d). In hypertrophic chondrocytes of *Runx2*$^{+/+}$ embryos, Runx2 was
225 predominantly localized in the nucleus (Fig. 5e, f). In contrast, many cells in *Runx2*$^{m/m}$ embryos
226 exhibited partial nuclear translocation, but cytoplasmic localization was also observed, and
227 overall nuclear localization of Runx2 was significantly reduced (Fig. 5g, h). Quantification of
228 the nuclear-to-total Runx2 fluorescence intensity ratio revealed a significant decrease in
229 *Runx2*$^{m/m}$ embryos compared to *Runx2*$^{+/+}$ embryos (Fig. 5i, Fig. S5).

230 These results indicate that the p.R232Q mutation in the RHD impairs Runx2 function in
231 skeletal development by reducing its expression, transcriptional activation capacity, and nuclear
232 localization.

233

234 Postnatal bone abnormalities recapitulating human CCD in *Runx2*$^{m/+}$ mice

235 *Runx2*$^{m/+}$ mice showed smaller body size and length at 1 month of (Fig. 6a) and 18.3% lower
236 body weight at 4 months compared to *Runx2*$^{+/+}$ mice (Fig. 6b). Three-dimensional (3D)
237 rendering images from micro-CT (μCT) scans revealed significantly smaller clavicles in
238 *Runx2*$^{m/+}$ mice (Fig. 6c), and skeletal preparations at 3 months confirmed markedly hypoplastic
239 clavicles and scapulae compared to *Runx2*$^{+/+}$ mice (Fig. 6d).

240 To investigate postnatal changes in cranial sutures over time, skulls of *Runx2*$^{+/+}$ and
241 *Runx2*$^{m/+}$ mice were analyzed at 1, 2, and 3 months of age using μCT, and 3D rendered images
242 were examined (Fig. 6e). At 1 month, while cranial sutures of *Runx2*$^{+/+}$ mice were nearly closed,
243 those in *Runx2*$^{m/+}$ mice remained open, showing delayed closure and Wormian bones at the
244 lambdoid suture (Fig. 6e). At 2 and 3 months, the sutures in *Runx2*$^{m/+}$ mice remained open with
245 persistent closure defects and Wormian bones, indicating impaired cranial ossification (Fig. 6e).
246 Consistently, skeletal preparations at 6 months showed that *Runx2*$^{m/+}$ mice had an open anterior
247 fontanelle, impaired suture closure, a short nasal apex, and zygomatic arch dysplasia, whereas
248 *Runx2*$^{+/+}$ mice had fully closed cranial sutures (Fig. 6f).

249 Taken together, these findings demonstrate that *Runx2*$^{m/+}$ mice carrying a clinically relevant
250 RHD missense mutation develop postnatal features of severe CCD.

251

252 Formation of accessory root-like protrusions in *Runx2*$^{m/+}$ mice

253 CCD patients often exhibit delayed eruption and supernumerary teeth[1], whereas supernumerary
254 teeth are absent in heterozygous *Runx2*-deficient mice[14]. Similarly, no supernumerary teeth
255 were observed in *Runx2*$^{m/+}$ mice; however, 3D rendering of μCT images revealed a previously
256 unreported accessory root-like protrusion between the three roots of the maxillary first molars
257 (Fig. 7a-d).

258 In mice, the maxillary first molars develop two buccal roots (mesial and distal) and one

259 palatal root, with root development coordinated through the independent growth of each root
260 from the furcation area via Hartwig's epithelial root sheath (HERS)[26]. The furcation process of
261 the mouse maxillary first molar begins with the formation of the distal buccal and palatal root,
262 followed by separation of the mesial buccal root and palatal roots, mediated through the fusion
263 of epithelial tongue-like processes formed by HERS[26]. To examine the development of the small
264 root-like protrusion, 3D μCT images of the maxillary first molars of *Runx2*$^{m/+}$ mice were
265 analyzed at 2, 3, 4, and 8 weeks (Fig. 7e-l). At 2 weeks, crown formation was complete, but
266 calcification at the root furcation area was incomplete, and three roots were not yet fully
267 separated (Fig. 7e, f). By 4 weeks, roots were clearly separated and elongated rapidly, with a
268 small protrusion forming near the furcation between the distal buccal and palatal roots (Fig. 7g-
269 j). At 8 weeks, root elongation continued, but the protrusion size remained unchanged (Fig. 7
270 k, l). Figure 7m illustrates the phenotype observed in this study alongside previous findings in
271 wild-type mice[26-28], and shows that in *Runx2*$^{m/+}$ mice, the epithelial processes fail to close
272 properly during root furcation, causing a small protrusion.
273 Hence, these results identify a previously unrecognized dental phenotype associated with
274 *Runx2* haploinsufficiency and provide new insights into the molecular mechanism underlying
275 root furcation.
276
277 **DISCUSSION**
278 This study presents the first *in vivo* functional analysis of pathological *Runx2* RHD mutations
279 using novel mouse lines carrying either a missense or a frameshift-induced dysfunctional RHD.
280 Clinically relevant *Runx2*$^{m/+}$ mice harboring p.R232Q corresponding human *RUNX2* p.R225Q,
281 exhibited skeletal abnormalities characteristic of classic CCD. Notably, this is the first *in vivo*
282 evidence that homozygous RHD mutations alone can completely abolish bone formation,

283 resulting in a skeleton composed entirely of cartilage. Although supernumerary teeth were
284 absent in heterozygous mutants, 3D μCT imaging revealed a novel accessory root-like
285 protrusion in the maxillary first molar during furcation. These findings demonstrate the
286 importance of modeling specific RHD mutations and provide new insights into the skeletal and
287 dental pathology of CCD beyond previous studies of *Runx2*-deficient mice.

288 Missense substitutions account for nearly half of all mutations reported in the Human
289 Gene Mutation Database[29]. Missense mutation p.R225Q is one of the most frequent across
290 diverse populations worldwide[14,17,19,30,31]. Arginine (R) residues, such as R225 in human
291 RUNX2 is crucial for protein stability through hydrogen bonds and salt bridges. Substitutions
292 of these residues can disrupt interactions with charged molecules like DNA and other proteins,
293 leading to pathogenic effects[32]. *In silico* analysis predicts that R225, a highly conserved residue
294 across species, forms two hydrogen bonds with E226, which are lost in mutant RUNX2[31].
295 Consistently, the equivalent mouse mutation p.R232Q abolishes osteocalcin promoter
296 activation due to loss of RHD function. In homozygous mice, expression of *Col10a1*[33,34], a
297 direct Runx2 target, was markedly reduced. The p.R232Q Runx2 failed to sustain *Runx2*
298 expression in hypertrophic chondrocytes, causing maturational arrest. In *Runx2*$^{\Delta 2/\Delta 2}$ mice, the
299 lack of bone formation results from loss of function, most likely due to nonsense-mediated
300 decay triggered by the frameshift mutation, consistent with previous reports that nonsense or
301 frameshift mutations also cause classic CCD[6,35,36].

302 Two *Runx2* knockout mouse lines have been previously reported: one generated by
303 disrupting the Q/A repeat domain with an *IRES-lacZ-pA* cassette[14], and another by deleting an
304 exon containing 41 amino acids of the RHD using a *PGK-neo* cassette[8]. In the latter line
305 carrying a LacZ reporter, X-gal staining showed persistent activity of the endogenous *Runx2*
306 promoter even in homozygotes, with blue staining in bone-forming regions[14]. However, the

307 prolonged half-life of LacZ hampers accurate tracking of the temporal dynamics of mutant
308 Runx2 expression during skeletogenesis. Indeed, *Runx2*$^{m/m}$ embryos exhibited markedly
309 reduced mutant Runx2 expression, suggesting that loss of functional Runx2 impairs either the
310 maintenance of its transcription or protein stability. These findings shed light on the *in vivo*
311 regulation and dynamics of Runx2 expression that are not captured by reporter-based
312 approaches.

313 The classical NLS typically comprises 5-20 amino acids rich in basic amino acid residues
314 like lysine (K) and arginine (R)[37]. Runx2 contains a Myc-related 9 amino acid NLS
315 (PRRHRQKLD) at the RHD-PST junction, essential for its nuclear localization[25]. Previous
316 studies using NIH-3T3, U2OS, C3H10T1/2, and HEK293T cells showed that wild-type
317 RUNX2 localizes to the nucleus, whereas p.R225Q or p.R225W mutants exhibited impaired
318 nuclear translocation[30,38]. Fusion proteins carrying p.R225Q or p.R225W mutation fail to
319 efficiently accumulate in the nucleus[30], unlike the wild-type. RUNX2 carrying either the
320 p.K218N or p.K220I mutation (previously described as K204N and T206I, respectively), both
321 located near the NLS, fails to translocate to the nucleus. In contrast, the p.R225Q mutant
322 (previously described as R211Q) shows approximately equal distribution between the nucleus
323 and cytoplasm in about half of the cells[38]. Although R232 in mouse Runx2 is located near the
324 NLS, its mutation caused only a partial defect in nuclear localization, with approximately 70%
325 of the mutant Runx2 detected in the nuclei of hypertrophic chondrocytes in *Runx2*$^{m/m}$ mice.
326 Thus, reduced function and expression due to RHD dysfunction, rather than impaired nuclear
327 localization, is likely the primary contributor to the skeletal phenotype. A missense mutation in
328 the RHD has been reported to exert a dominant-negative effect[39], which may explain the
329 observation that the mineralized area is smaller in missense mutant compared to the frameshift
330 mutant.

331 In CCD patients, supernumerary teeth most commonly develop in the incisors and
332 premolars[40]. In contrast, mice have a monomorphic dentition with one continuously growing
333 incisor and three molars, separated by a toothless diastema, lacking canines or premolars[41].
334 Unlike the dimorphic dentition of humans, tooth eruption in *Runx2*-deficient mice is only
335 slightly delayed or not significantly affected[11,42], similar to the normal eruption of deciduous
336 teeth in CCD patients[2,43,44]. These species-specific differences in dental architecture may
337 explain why the dental phenotype in mice is less pronounced than the skeletal phenotype.

338 We identified an accessory root-like protrusion in the maxillary first molars of *Runx2*$^{m/+}$
339 mice, representing a novel dental phenotype distinct from previously reported abnormalities
340 such as short roots or taurodontism[45]. In normal maxillary molars, horizontal differential growth
341 of HERS forms three tongue-like interradicular processes that fuse to divide the single cervical
342 opening into three parts, initiating multi-root formation[26,46]. The accessory roots likely result
343 from impaired fusion of these processes at the leading edge of HERS, caused by *Runx2*
344 haploinsufficiency (Fig. 7m). As Runx2 is critical for epithelial-mesenchymal interactions
345 during root development, reduced expression may disrupt spatiotemporal regulation of HERS
346 fusion during furcation, leading to protrusion formation. Notably, this protrusion was much
347 smaller than normal roots, suggesting incomplete root elongation, possibly due to aberrant
348 odontoblast differentiation. Given that maxillary first molars normally have three roots and the
349 most complex furcation among molars, their intricate morphology and spongy maxillary bone
350 structure may underlie susceptibility to furcation abnormalities in *Runx2*$^{m/+}$ mice.

351 In conclusion, our *Runx2* mutant mice replicate key skeletal features of CCD and uncover
352 a novel dental phenotype characterized by accessory roots, likely resulting from impaired root
353 furcation. Although unconfirmed in humans, homozygous mutants in mice exhibited a complete
354 lack of bone formation. These findings highlight the critical role of the RHD in both skeletal

355 and multi-root development, providing new insights into CCD pathogenesis.

356

357 **MATERIALS AND METHODS**

358 Animals

359 C57BL/6 mice were purchased from CLEA Japan, Inc. (Tokyo, Japan) and bred for experiments.
360 All procedures were approved by the Animal Care Committee of the Institute for Frontier Life
361 and Medical Sciences, Kyoto University, as well as the Committee of Animal Experimentation
362 and the Recombinant DNA Committee of Hiroshima University.

363

364 Generation of TALEN-mediated *Runx2* mutant mouse lines

365 TALEN plasmids targeting mouse *Runx2* were constructed using the Platinum Gate TALEN
366 Kit (Addgene, Watertown, MA) as previously described[47]. After linearization of TALEN
367 plasmids for *Runx2-TALEN-R* and *-L* with SmaI, mRNAs were synthesized using the
368 mMESSAGE mMACHINE T7 ULTRA Kit (Thermo Fisher Scientific, Waltham, MA) and
369 purified with the MEGAclear kit (Thermo Fisher Scientific). The TALEN mRNAs and an
370 ssODN carrying the p.R232Q and a silent ApaI site were microinjected into C57BL/6 oocytes.
371 Injected eggs were transferred into pseudopregnant ICR females. Genotyping was performed
372 by PCR on genomic DNA extracted from earpieces using specific primers (Table S3). The
373 products were digested with SmaI and ApaI, and confirmed by direct sequencing using the
374 BigDye Terminator Cycle Sequencing kit and an ABI 3100 Genetic Analyzer (Applied
375 Biosystems, Thermo Fisher Scientific). Fragments were analyzed by agarose gel
376 electrophoresis or a microchip electrophoresis system for DNA/RNA analysis (MultiNA,
377 SHIMADZU, Kyoto, Japan).

378

379 Skeletal preparation

380 Whole-mount skeletal staining was performed as previously described[48,49]. Embryos or mice
381 were skinned, fixed in ethanol, stained with Alcian blue 8GX (Sigma-Aldrich, Merck KGaA,
382 Darmstadt, Germany), washed with ethanol, and cleared in 1% KOH. Samples were then
383 stained with 0.05% Alizarin Red S (Sigma-Aldrich) in 1% KOH, followed by additional
384 clearing in 1% KOH. Images were acquired using a MZ16 FA stereomicroscope equipped with
385 a DFC7000 T camera (Leica Microsystems (Leica), Wetzlar, Germany).

386

387 Tissue sections

388 For frozen sections, embryos were fixed in 4% paraformaldehyde (PFA) in phosphate buffered
389 saline (PFA/PBS), infiltrated with 20% sucrose/PBS, embedded in Tissue Tek O.C.T compound
390 (Sakura Finetek, Tokyo, Japan), sectioned at 4-6 μm. For paraffin sections, embryos were fixed
391 in 4% PFA/PBS, decalcified with Morse's solution[50], dehydrated, immersed in methyl benzoate
392 (Nacalai Tesque, Kyoto, Japan), embedded in paraffin (Thermo Fisher Scientific), sectioned at
393 6 μm.

394

395 Histological staining

396 Frozen sections were stained with ALP substrate solution of TRAP/ALP Stain Kit (FUJIFILM
397 Wako Pure Chemical Corporation (FUJIFILM Wako), Osaka, Japan), or stained with 1%
398 alizarin red (Muto Pure Chemicals, Tokyo, Japan). For toluidine blue staining, deparaffinized
399 and hydrated sections were stained with 0.05% toluidine blue solution (pH 4.1; Muto Pure
400 Chemicals).

401

402 *In situ* hybridization

403 Digoxygenin (DIG)- labelled RNA probes for *Col2a1*, *Acan*[51], *Ihh*, *Col10a1*[52], *Runx2*[33], *Spp1*[53]
404 and *Col1a1*[54] were synthesized using a DIG RNA labelling kit (F. Hoffmann-La Roche Ltd.
405 (Roche), Basel, Switzerland). Mouse *Col2a1* and *Ihh* cDNA were amplified by RT-PCR using
406 the following primers (Table S3). Paraffin sections were deparaffinized, rehydrated and treated
407 with 10 μg/mL Proteinase K (Roche), followed by post-fixation with 4% PFA/PBS for 10 min.
408 Sections were hybridized with DIG-labeled RNA probes at 65°C for 16 h, washed, and
409 incubated with anti-DIG Fab fragment conjugated with alkaline phosphatase (anti-DIG-AP;
410 Roche) and BM purple (Roche). Counterstaining was performed with eosin (Sakura Finetek).
411
412 μCT imaging
413 Mice were anesthetized with a combination of medetomidine, midazolam, and butorphanol (0.1
414 mL per 10 g body weight). Calvaria and clavicle were scanned with SkyScan1176 (Bruker,
415 Antwerp, Belgium; 17.5 μm resolution, 50 kV and 500 μA), and teeth were scanned with
416 CosmoScan GXIII (Rigaku Holdings Corporation, Tokyo, Japan; 12.9 μm resolution, 100 kV
417 and 120 μA). 3D rendering was performed using Amira software (Thermo Fisher Scientific,
418 version 2021.1).
419
420 Plasmid construction
421 Mouse Runx2 cDNA was amplified from *pSG5-mRunx2* and cloned into the EcoRI site of
422 pcDNA-FLAG[51] to generate *pcDNA3 Runx2 WT* using primers. Mutant vectors carrying the
423 p.R232Q, p.R232W, or p.R200X mutations (*pcDNA3 Runx2 RQ*, *RW*, and *RX*, respectively)
424 were generated by inverse-PCR with KOD Plus DNA polymerase (TOYOBO, Osaka, Japan)
425 using *pcDNA3 Runx2 WT* as the template. See Table S2 for primers.
426

427 Dual luciferase reporter assay

428 HEK293T cells (Takara Bio Inc., Shiga, Japan) were cultured in Dulbecco's modified Eagle's
429 medium with high glucose (Sigma-Aldrich) supplemented with 10% heat-inactivated-FBS
430 (Hana-Nesco Bio Corp., Osaka, Japan), 2 mM L-glutamine (FUJIFILM Wako), and 50 mg/mL
431 kanamycin (Sigma-Aldrich) at 37°C in 5% CO_2. Cells were transiently transfected with
432 *p6OSE2-luc*[23] and *pGL4.10[luc2]*, *pGL4.74[hRluc/TK]* (Promega, Madison, WI), and *pcDNA3*
433 *Runx2 WT or mutant* vectors. Transfection was performed using Lipofectamine LTX Reagent
434 or Lipofectamine 3000 Reagent (Thermo Fisher Scientific). After 48 h, luciferase activities
435 were measured using the PicaGene Dual Sea Pansy Luminescence Kit (Toyo ink, Tokyo, Japan)
436 and Centro XS^3 LB 960 (Berthold Technologies, Bad Wildbad, Germany).

437

438 Western blotting

439 Forelimbs were frozen in liquid nitrogen, crashed using SK mill (SK-200, Tokken,Inc, Chiba,
440 Japan), and lysed in 8 M urea extraction buffer [8 M urea, 50 mM Tris-HCl (pH 8.0), 1 mM
441 DTT and 1 mM EDTA]. HEK293T cells were transfected with WT or mutant Runx2 vector
442 using Lipofectamine 3000 Reagent (Thermo Fisher Scientific), and lysed in 8 M urea extraction
443 buffer. Protein concentrations were determined using BCA Protein Assay Kit (Thermo Fisher
444 Scientific), and samples were mixed with 6x SDS sample buffer (Nacalai tesque, Inc., Kyoto,
445 Japan), boiled, and loaded onto a 10% SDS-polyacrylamide gels (e-PAGEL, ATTO, Tokyo,
446 Japan). Samples were separated by SDS-PAGE and transferred to PVDF membranes using
447 iBlot3 (Invitrogen). Membrane were blocked with 3% skim milk (FUJIFILM Wako) in Tris-
448 buffered saline with 0.05% Tween 20 (TBS-T), incubated with rabbit anti-Runx2 monoclonal
449 antibody (1:1250, Cell Signalling Technology, Danvers, MA) and mouse anti-β-actin
450 monoclonal antibody (1:1250, FUJIFILM Wako) overnight, then with IRDye 680RD Goat anti-

451 Rabbit IgG and IRDye 800CW Goat anti-Mouse IgG (1:15000, LI-COR, Lincoln, NE). Bands
452 were visualized using Odyssey CLx (LI-COR).
453
454 Immunostaining
455 Frozen sections were subjected to antigen retrieval in sodium citrate buffer (pH6.0) by
456 microwave heating, followed by permeabilization with 0.2% TritonX-100 (Sigma-Aldrich).
457 After blocking with 2% skim milk/PBS, sections were incubated with rabbit anti-Runx2
458 monoclonal antibody (1:1600, Cell Signaling Technology) or rabbit anti-Collagen X
459 monoclonal antibody (1:500, Abcam, Cambridge, UK) overnight, washed with PBS, and
460 incubated with Goat anti-Rabbit IgG (H+L) Highly Cross-Adsorbed Secondary antibody
461 conjugated with Alexa Fluor Plus 594 (1:500, Thermo Fisher Scientific). Nuclei were
462 counterstained with 4',6-diamidino-2-phenylindole (DAPI) (Sigma-Aldrich). Stained sections
463 were mounted using VECTASHIELD Hard-Set Mounting Medium (Vector Laboratories, Inc.,
464 Newark, CA). Images were acquired using DMRXA microscope with DFC310 FX Camera and
465 Stellaris 5 confocal laser scanning microscope (Leica).
466
467 Image analysis
468 To analyze Runx2 nuclear localization, maximum projection images were generated from
469 confocal images using LAS X software (Leica). Cells in the Col10^{+} hypertrophic cartilage layer
470 were analyzed with ImageJ software (National Institutes of Health, Bethesda, MD). Regions of
471 interest (ROIs) for whole-cell Runx2 [ROIs(r)] were defined from Runx2 signals using
472 thresholding based on the Huang algorithm[55]. Nuclear regions of interest [ROIs(d)] were
473 defined from DAPI images with thresholds set using the Default (IsoData) algorithm[56],
474 excluding ROIs smaller than 50 pixels. ROIs(r) and ROIs(d) were overlayed on Runx2 images,

475 and the respective Runx2 intensities in whole cells and nuclei were measured using Integrated
476 Density. Nuclear localization was calculated as: %Nuclear = (Runx2 intensity in nucleus/Runx2
477 intensity in the whole cell) ×100. Only cells with overlapping ROI(r) and ROI(d), confirmed
478 by visual inspection, were included. Multiple ROI(d) within one ROI(r) were summed.
479
480 Statistical analysis
481 Statistical significance between two groups was determined using Student's *t*-test or Mann-
482 Whitney U test. Comparisons among multiple groups were performed by one-way analysis of
483 variance (ANOVA) followed by Tukey's multiple comparison test. Graphpad Prism 10
484 (Dotmatics, Boston, MA, version 10. 2. 3) was used.
485
486 **DATA AVAILABILITY**
487 All data associated with this study are available upon request.
488
489 **ACKNOWLEDGEMENTS**
490 Plasmids for mouse *Col10a1, Runx2* (including *pSG5-mRunx2*), and *Spp1* were generously
491 provided by Dr. Bjorn R Olsen (Harvard Medical School), Dr. Toshihisa Komori (Nagasaki
492 University), and Dr. Shinsuke Ohba (Osaka University), respectively. The *p6OSE2-luc* vector
493 was obtained from Dr. Karsenty (Columbia University) through Dr. Kenji Hata (Osaka
494 University). We thank Drs. Kosuke Hosoba and Xynyi Yu for their technical assistance. Parts
495 of this work was performed using the facilities at the Natural Science Center for Basic Research
496 and Development and the Central Laboratory, Faculty of Dentistry, Hiroshima University. This
497 study was supported by the Japan Society for the Promotion of Science Grants-in-Aid for
498 Scientific Research (Grant Numbers: 16K15780, 21KK0161, 22K10148, 25K13145); the

Frontier Development Program for Genome Editing funded by the Doctoral Program for Worldleading Innovative and Smart Education, JST SPRING (Grant Number JPMJSP2132); and the Cooperative Research Program of the Institute for Frontier Life and Medical Sciences, Kyoto University, Japan.

COMPETING INTERESTS

The authors declare no competing or financial interests.

AUTHOR CONTRIBUTIONS

C.S. designed the research; S.Ogawa, S.H., Y.Y., M.H., C.S., A.H., H.W., T.S., K.H., S.Ogata, K.F., and G.K. performed the experiments; C.S., S.Ogawa, S.H., Y.Y., A.H., S.M., and T.S. analyzed data; C.S., S.Ogawa, S.H., and Y.Y. wrote the paper; C.S., S.M., K.U., T.O., K.T., and D.D. provided feedback and guidance; S.M., A.H., T.S., K.F., T.O., T.Y., R.K., Y.S., and D.D. reviewed and edited the manuscript.

REFERENCES

1 Mundlos, S. Cleidocranial dysplasia: clinical and molecular genetics. *J Med Genet*. **36**, 177-182 (1999).

2 Mundlos, S. *et al.* Mutations involving the transcription factor CBFA1 cause cleidocranial dysplasia. *Cell*. **89**, 773-779 (1997).

3 Cooper, S. C., Flaitz, C. M., Johnston, D. A., Lee, B. & Hecht, J. T. A natural history of cleidocranial dysplasia. *Am J Med Genet*. **104**, 1-6 (2001).

4 Jensen, B. L. & Kreiborg, S. Dental treatment strategies in cleidocranial dysplasia. *Br Dent J*. **172**, 243-247 (1992).

523 5 Kreiborg, S. & Jensen, B. L. Tooth formation and eruption - lessons learnt from
524 cleidocranial dysplasia. *Eur J Oral Sci*. **126 Suppl 1**, 72-80 (2018).
525 6 Lou, Y. *et al.* A Runx2 threshold for the cleidocranial dysplasia phenotype. *Human*
526 *Molecular Genetics*. **18**, 3, 556-568 (2009).
527 7 Jaruga, A., Hordyjewska, E., Kandzierski, G. & Tylzanowski, P. Cleidocranial dysplasia
528 and RUNX2-clinical phenotype-genotype correlation. *Clin Genet*. **90**, 393-402 (2016).
529 8 Komori, T. *et al.* Targeted disruption of Cbfa1 results in a complete lack of bone
530 formation owing to maturational arrest of osteoblasts. *Cell*. **89**, 755-764 (1997).
531 9 Qin, X. *et al.* Runx2 is essential for the transdifferentiation of chondrocytes into
532 osteoblasts. *Plos Genet*. **16**, 11, e1009169 (2020).
533 10 Komori, T. Whole Aspect of Runx2 Functions in Skeletal Development. *Int J Mol Sci*.
534 **23**, 5776 (2022).
535 11 Yoda, S., Suda, N., Kitahara, Y., Komori, T. & Ohyama, K. Delayed tooth eruption and
536 suppressed osteoclast number in the eruption pathway of heterozygous Runx2/Cbfa1
537 knockout mice. *Archives of Oral Biology*. **49**, 435-442 (2004).
538 12 Bruderer, M., Richards, R. G., Alini, M. & Stoddart, M. J. Role and regulation of
539 RUNX2 in osteogenesis. *Eur Cell Mater*. **28**, 269-286 (2014).
540 13 Yang, L. *et al.* Whole-exome sequencing of a novel initiation codon mutation in RUNX2
541 in a Chinese family with cleidocranial dysplasia. *Medicine (Baltimore)*. **100**, e27746
542 (2021).
543 14 Otto, F. *et al.* Cbfa1, a candidate gene for cleidocranial dysplasia syndrome, is essential
544 for osteoblast differentiation and bone development. *Cell*. **89**, 765-771 (1997).
545 15 Yoshida, T. *et al.* Functional analysis of RUNX2 mutations in cleidocranial dysplasia:
546 novel insights into genotype-phenotype correlations. *Blood Cells Mol Dis*. **30**, 184-193

547 (2003).

548 16 Saito, A. *et al.* Targeted reversion of induced pluripotent stem cells from patients with
549 human cleidocranial dysplasia improves bone regeneration in a rat calvarial bone defect
550 model. *Stem Cell Res Ther*. **9**, 12 (2018).

551 17 Yamasaki, S. *et al.* Generation of cleidocranial dysplasia-specific human induced
552 pluripotent stem cells in completely serum-, feeder-, and integration-free culture. *In*
553 *Vitro Cellular and Developmental Biology - Animal*. **52**, 252-264 (2016).

554 18 Hamada, A. *et al.* Identification of a familial cleidocranial dysplasia with a novel
555 RUNX2 mutation and establishment of patient-derived induced pluripotent stem cells.
556 *Odontology*. **110**, 444-451 (2022).

557 19 Wu, L. Z. *et al.* Role of the RUNX2 p.R225Q mutation in cleidocranial dysplasia: A
558 rare presentation and an analysis of the RUNX2 protein structure. *Genetics and*
559 *Molecular Research*. **13**, 1, 1187-1194 (2014).

560 20 Lee, K. E. *et al.* RUNX2 mutations in cleidocranial dysplasia. *Genet Mol Res*. **12**, 4567-
561 4574 (2013).

562 21 Suda, N. *et al.* Correlation between genotype and supernumerary tooth formation in
563 cleidocranial dysplasia. *Orthod Craniofac Res*. **13**, 197-202 (2010).

564 22 Brubaker, K. D., Vessella, R. L., Brown, L. G. & Corey, E. Prostate cancer expression
565 of runt-domain transcription factor Runx2, a key regulator of osteoblast differentiation
566 and function. *Prostate*. **56**, 13-22 (2003).

567 23 Ducy, P., Zhang, R., Geoffroy, V., Ridall, A. L. & Karsenty, G. Osf2/Cbfa1: a
568 transcriptional activator of osteoblast differentiation. *Cell*. **89**, 747-754 (1997).

569 24 Geoffroy, V., Ducy, P. & Karsenty, G. A PEBP2 alpha/AML-1-related factor increases
570 osteocalcin promoter activity through its binding to an osteoblast-specific cis-acting

element. *J Biol Chem*. **270**, 30973-30979 (1995).

25 Thirunavukkarasu, K., Mahajan, M., McLarren, K. W., Stifani, S. & Karsenty, G. Two domains unique to osteoblast-specific transcription factor Osf2/Cbfa1 contribute to its transactivation function and its inability to heterodimerize with Cbfbeta. *Mol Cell Biol*. **18**, 4197-4208 (1998).

26 Li, J., Parada, C. & Chai, Y. Cellular and molecular mechanisms of tooth root development. *Development*. **144**, 374-384 (2017). Japanease.

27 Fujita, Y. Formation of subpulpal wall in mouse maxillary first molar. *Jpn. J. Oral Biol*. **20**, 221-228 (1978).

28 Seo, H. *et al.* Regulation of root patterns in mammalian teeth. *Sci Rep*. **7**, 12714 (2017).

29 Stenson, P. D. *et al.* The Human Gene Mutation Database: towards a comprehensive repository of inherited mutation data for medical research, genetic diagnosis and next-generation sequencing studies. *Hum Genet*. **136**, 665-677 (2017).

30 Quack, I. *et al.* Mutation analysis of core binding factor A1 in patients with cleidocranial dysplasia. *Am J Hum Genet*. **65**, 1268-1278 (1999).

31 López, J. T. *et al.* New Genetic Variants of RUNX2 in Mexican Families Cause Cleidocranial Dysplasia. *Biology*. **13**, 173 (2024).

32 Pandey, P. & Alexov, E. Most Monogenic Disorders Are Caused by Mutations Altering Protein Folding Free Energy. *Int J Mol Sci*. **25**, 1963 (2024).

33 Inada, M. *et al.* Maturational disturbance of chondrocytes in Cbfa1-deficient mice. *Dev Dyn*. **214**, 279-290 (1999).

34 Kim, I. S., Otto, F., Zabel, B. & Mundlos, S. Regulation of chondrocyte differentiation by Cbfa1. *Mech Dev*. **80**, 159-170 (1999).

35 Xuan, D. *et al.* Effect of cleidocranial dysplasia-related novel mutation of RUNX2 on

595 characteristics of dental pulp cells and tooth development. *J Cell Biochem*. **111**, 1473-
596 1481 (2010).
597 36 Huang, Y. *et al.* Novel RUNX2 frameshift mutations in Chinese patients with
598 cleidocranial dysplasia. *Eur J Oral Sci*. **121**, 142-147 (2013).
599 37 Dingwall, C. & Laskey, R. A. Nuclear targeting sequences--a consensus? *Trends*
600 *Biochem Sci*. **16**, 478-481 (1991).
601 38 Yoshida, T. *et al.* Functional analysis of RUNX2 mutations in Japanese patients with
602 cleidocranial dysplasia demonstrates novel genotype-phenotype correlations. *Am J Hum*
603 *Genet*. **71**, 724-738 (2002).
604 39 Puppin, C. *et al.* Functional analysis of a novel RUNX2 missense mutation found in a
605 family with cleidocranial dysplasia. *J Hum Genet*. **50**, 679-683 (2005).
606 40 Lu, Y., Wang, J., Li, L. & Zhang, X. Three-dimensional evaluation of dental
607 characteristics in patients with Cleidocranial dysplasia. *BMC Oral Health*. **24**, 572
608 (2024).
609 41 Peterkova, R., Lesot, H. & Peterka, M. Phylogenetic memory of developing mammalian
610 dentition. *J Exp Zool B Mol Dev Evol*. **306**, 234-250 (2006).
611 42 Zou, S. J., D'Souza, R. N., Ahlberg, T. & Bronckers, A. L. Tooth eruption and cementum
612 formation in the Runx2/Cbfa1 heterozygous mouse. *Arch Oral Biol*. **48**, 673-677 (2003).
613 43 Jensen, B. L. & Kreiborg, S. Development of the dentition in cleidocranial dysplasia. *J*
614 *Oral Pathol Med*. **19**, 89-93 (1990).
615 44 Seow, W. K. & Hertzberg, J. Dental development and molar root length in children with
616 cleidocranial dysplasia. *Pediatr Dent*. **17**, 101-105 (1995).
617 45 Wang, J. & Feng, J. Q. Signaling Pathways Critical for Tooth Root Formation. *J Dent*
618 *Res*. **96**, 1221-1228 (2017).

619 46 Kumar, G. S. in *Orban's Oral Histology and Embryology* (ed G. S. Kumar) Ch. 3,
620 (Elsevier, 2019).
621 47 Sakuma, T. *et al.* Repeating pattern of non-RVD variations in DNA-binding modules
622 enhances TALEN activity. *Sci Rep*. **3**, 3379 (2013).
623 48 Rigueur, D. & Lyons, K. M. Whole-mount skeletal staining. *Methods Mol Biol*. **1130**,
624 113-121 (2014).
625 49 Sugimoto, Y. *et al.* Scx+/Sox9+ progenitors contribute to the establishment of the
626 junction between cartilage and tendon/ligament. *Development*. **140**, 2280-2288 (2013).
627 50 Shibata, Y., Fujita, S., Takahashi, H., Yamaguchi, A. & Koji, T. Assessment of
628 decalcifying protocols for detection of specific RNA by non-radioactive in situ
629 hybridization in calcified tissues. *Histochem Cell Biol*. **113**, 153-159 (2000).
630 51 Takimoto, A. *et al.* Differential transactivation of the upstream aggrecan enhancer
631 regulated by PAX1/9 depends on SOX9-driven transactivation. *Sci Rep*. **9**, 4605 (2019).
632 52 Apte, S. S., Seldin, M. F., Hayashi, M. & Olsen, B. R. Cloning of the human and mouse
633 type X collagen genes and mapping of the mouse type X collagen gene to chromosome
634 10. *Eur J Biochem*. **206**, 217-224 (1992).
635 53 Bastepe, M. *et al.* Stimulatory G protein directly regulates hypertrophic differentiation
636 of growth plate cartilage in vivo. *Proc Natl Acad Sci U S A*. **101**, 14794-14799 (2004).
637 54 Yoshimoto, Y. *et al.* Scleraxis is required for maturation of tissue domains for proper
638 integration of the musculoskeletal system. *Sci. Rep.* **7**, 45010 (2017).
639 55 Huang, L.-K. & Wnag, M.-J. J. Image thresholding by minimizing the measures of
640 fuzziness. *Pattern Recognition*. **28**, 41-51 (1995).
641 56 Ridler, T. W. & Calvard, S. Picture Thresholding using an iterative selection method.
642 *IEEE Transactions on Systems, Man, and Cybernetics*. **8**, 630-632 (1978).
643

644 **LEGENDS**

645 **Fig. 1** Generation of *Runx2* mutant mice using Platinum TALENs.

646 **a** Schematic representation of the mouse *Runx2* gene with eight exons (labeled E1-E8 below),
647 distal (P1) and proximal (P2) promoters for Type II (MASNSL) and Type I (MRIVD) isoforms,
648 and target sites of Platinum TALENs (*mRunx2-TALEN-L* and *-R*). A 10 kb scale bar is shown.
649 The SmaI site (red box) includes G695 (underlined). The ssODN contains target sites (green),
650 a T>G silent mutation at 690 creating an ApaI site (blue box), and a G>A mutation at 695
651 disrupting the SmaI site. **b** Domain structure of the mRunx2 Type II protein (528 aa) and its
652 corresponding exons. The protein comprises a QA repeat domain, RHD, NLS, PST-rich domain,
653 NMTS, and a C-terminal VWRPY motif. Amino acid positions are indicated above, and the
654 corresponding exons (E1-E8) are shown below. **c** Nucleotide sequences are shown for the wild-
655 type (*Wt*, 670-725), missense mutant (*m*, c.695G>A; p.R232Q, 670-725), and two-base deletion
656 (*Δ2*, c.697_698delGA; p.E233TfsTer9, 670-723) alleles. *Wt* is on top, *m* in the middle, and *Δ2*
657 at the bottom. **d** Representative electropherograms of the targeted *Runx2* region in $Runx2^{+/+}$,
658 $Runx2^{m/+}$, and $Runx2^{\Delta 2/+}$ mice. A black arrow marks T at 690 in $Runx2^{+/+}$and $Runx2^{m/+}$ mice. A
659 blue arrow indicates overlapping T and A peaks at 690 in $Runx2^{m/+}$ mice, and a red arrow shows
660 overlapping A and G peaks at position 695 in $Runx2^{m/+}$ mice.

661

662 **Fig. 2** Skeletal phenotypes of *Runx2* mutant mice.

663 **a-j** Skeletal preparations of $Runx2^{+/+}$ (**a, f, g**), $Runx2^{m/+}$ (**b, h, i**), $Runx2^{\Delta 2/+}$ (**c**), $Runx2^{m/m}$ (**d, j**),
664 and $Runx2^{\Delta 2/\Delta 2}$ (**e**) mice at E18.5. Lateral views of embryos (**a-e**), clavicles (**g, i**) and dorsal
665 views of the calvaria (**f, h, j**) are presented. A white arrow indicates weak calcification. Scale
666 bars, 2 mm.

667

668 **Fig. 3** Histology and *in situ* hybridization of forearms in wild-type and *Runx2* mutant mice.

669 **a-c** TB, ALP, and AR staining of forearms prepared from *Runx2*$^{+/+}$, *Runx2*$^{m/+}$, *Runx2*$^{m/m}$ and

670 *Runx2*$^{\Delta 2/\Delta 2}$ embryos at E18.5. **d-j** Expression of *Col2a1* (**d**), *Acan* (**e**), *Ihh* (**f**), *Col10a1* (**g**),

671 *Runx2* (**h**), *Spp1* (**i**), and *Col1a1* (**j**) in the forearm of *Runx2*$^{+/+}$, *Runx2*$^{m/+}$, or *Runx2*$^{m/m}$ embryos

672 at E18.5. Blue arrowheads in (**f**), (**g**), and (**i**) mark prehypertrophic/hypertrophic chondrocytes.

673 A red arrowhead in (**h**) indicates the perichondrium. Scale bars, 500 μm.

674

675 **Fig. 4** Expression and transcriptional activity of wild-type and mutant Runx2.

676 **a** Expression of wild-type and missense mutant Runx2 in HEK293T cells. Cells were

677 transfected with an empty vector as the control, wild-type *Runx2,* or the *Runx2 RQ* mutant

678 construct, all using the pcDNA3 vector. **b** Expression of Runx2 in forelimb extracts from

679 *Runx2*$^{+/+}$, *Runx2*$^{m/+}$ and *Runx2*$^{m/m}$ mice at E18.5. β-Actin was used as a loading control in both

680 **a** and **b**. **c** Dual luciferase assay in HEK293T cells co-transfected with the *p6OSE2-luc* reporter

681 vector and either empty vector, *Runx2 WT, Runx2 RQ, RW, or RX* mutant constructs using the

682 *pcDNA3 vector*. *pGL4.74[hRluc/TK]* was also co-transfected for normalization. Values for each

683 of five wells were normalized to *pGL4.74[hRluc/TK]* and are shown as fold induction relative

684 to the empty vector. Data present one of ≧3 independent experiments (mean ± SD, n=3). ****P

685 < 0.0001 *vs. Runx2 WT*.

686

687 **Fig. 5** Altered expression and subcellular localization of mutant Runx2 in chondrocytes.

688 **a-d** Immunostaining of Col10 (**a, c**) and Runx2 (**b, d**) proteins in the ulna of *Runx2*$^{+/+}$ and

689 *Runx2*$^{m/m}$ embryos at E18.5. Nuclei are counterstained with DAPI. Yellow boxes in (**a**) and (**c**)

690 indicate the Col10^{+} prehypertrophic/hypertrophic cartilage zone. The corresponding regions to

691 them are shown in the semi-serial sections in (**b**) and (**d**). The number of cells in the yellow

692 boxes of (**a**) and (**c**) indicating Col10^{+} region differs between *Runx2*$^{+/+}$ and *Runx2*$^{m/m}$. **e-h**
693 Confocal images of wild-type and mutant Runx2 (red) and nuclei (blue) in
694 prehypertrophic/hypertrophic chondrocytes. Representative localization patterns of wild-type
695 (**e, f**) and mutant (**g, h**) Runx2 are highlighted by rectangles and shown in insets. **i** Nuclear
696 localization rate of Runx2 in chondrocytes of the ulna in *Runx2*$^{+/+}$ and *Runx2*$^{m/m}$ embryos.
697 Runx2 signal intensities in the whole-cell (dashed regions in f and h) and those in nucleus were
698 quantified using imageJ. Data are means ± SD (*Runx2*$^{+/+}$, n = 88 cells; *Runx2*$^{m/m}$, n = 45 cells).
699 ****$P < 0.0001$ (Mann-Whitney *U*-test). Scale bars, 200 μm (a-d), 50 μm (e-h).
700
701 **Fig. 6** Postnatal skeletal development in *Runx2*$^{+/+}$ and *Runx2*$^{m/+}$ mice.
702 **a** Gross appearance of *Runx2*$^{+/+}$ and *Runx2*$^{m/+}$ mice at P30. **b** Body weight of *Runx2*$^{+/+}$ and
703 *Runx2*$^{m/+}$ mice at 16 weeks (n=3). *$P < 0.05$ *vs.* *Runx2*$^{+/+}$ (unpaired Student's *t*-test). **c** μCT-
704 based 3D reconstruction images of the axial and appendicular skeleton in the upper body of 3-
705 month-old *Runx2*$^{+/+}$ and *Runx2*$^{m/+}$ mice. **d** Skeletal preparations of the pectoral girdle and upper
706 limb in *Runx2*$^{+/+}$ and *Runx2*$^{m/+}$ mice at 6 months. **e** μCT-based 3D reconstruction images of the
707 calvaria in *Runx2*$^{+/+}$ and *Runx2*$^{m/+}$ mice at 1, 2, and 3 months. **f** Skeletal preparations of the
708 skull from *Runx2*$^{+/+}$ and *Runx2*$^{m/+}$ mice at 6 months. Abbreviations: sc, scapula; cl, clavicle; hu,
709 humerus; f, frontal bone; p, parietal bone; ip, interparietal bone; o, occipital bone. Scale bars, 5
710 mm.
711
712 **Fig. 7** Dental phenotypes of postnatal *Runx2* missense mice.
713 **a-d** 3D μCT images of the maxilla and mandible in *Runx2*$^{+/+}$ and *Runx2*$^{m/+}$ mice at 3 months.
714 Panels (**a**) and (**c**) show whole jaw views. Panels (**b**) and (**d**) show slice images with overlayed
715 3D reconstructions of the maxillary first molar. Insets display enlarged views of the molars. A

716 red arrow in (**d**) indicates an additional root-like structure. Scale bars, 2 mm. **e-l** 3D μCT images
717 of the right maxillary first molars in *Runx2*$^{m/+}$ mice at 2, 3, 4, and 8 weeks. Axial (**e, g, i, k**) and
718 corresponding sagittal (**f, h, j, l**) views from the same individuals are shown. Orange lines in
719 axial panels indicate the sagittal section planes. Directional arrows indicate the palatal (P),
720 buccal (B), apical (A), occlusal (O), distal (D) and mesial (M) directions. Images are from the
721 same individuals (n=3). **m** Schematic illustration of root furcation in *Runx2*$^{+/+}$ and *Runx2*$^{m/+}$
722 mice. Horizontal (top) and sagittal (bottom) views are shown, with orange lines in (**e-k**)
723 indicating the sagittal section planes. Tissue types are presented by pattern-filled squares. The
724 green panel shows the fusion of three epithelial processes (two buccal and one palatal) at P9,
725 P11, and P12. The blue and pink panels depict the progression of root furcation at 2, 3, and 4
726 weeks in *Runx2*$^{+/+}$ and *Runx2*$^{m/+}$ mice, respectively.

Figure 1

a

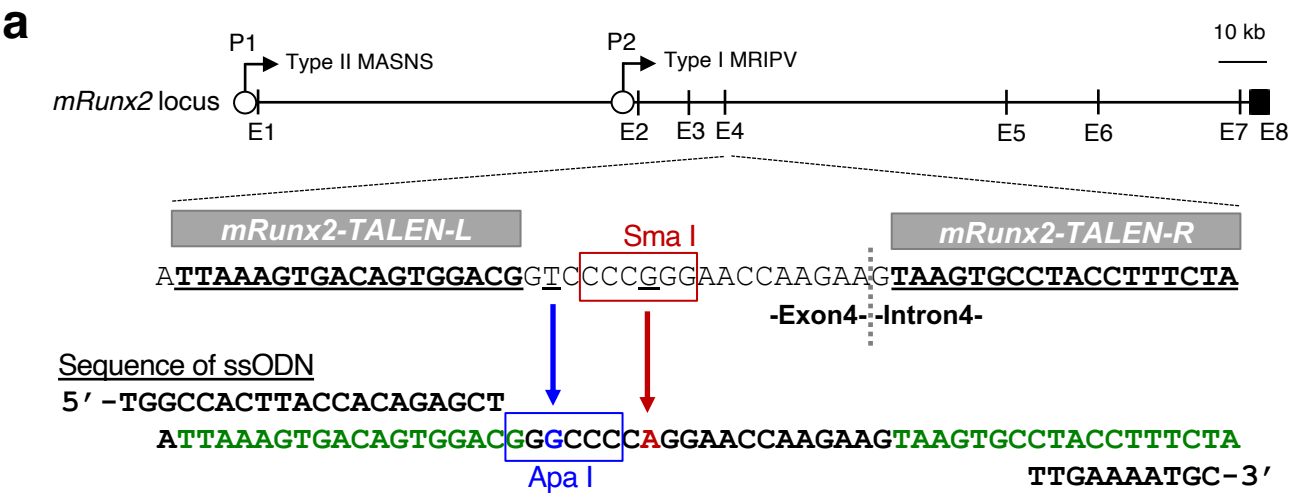

b

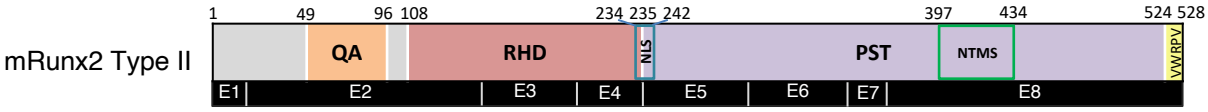

c

d

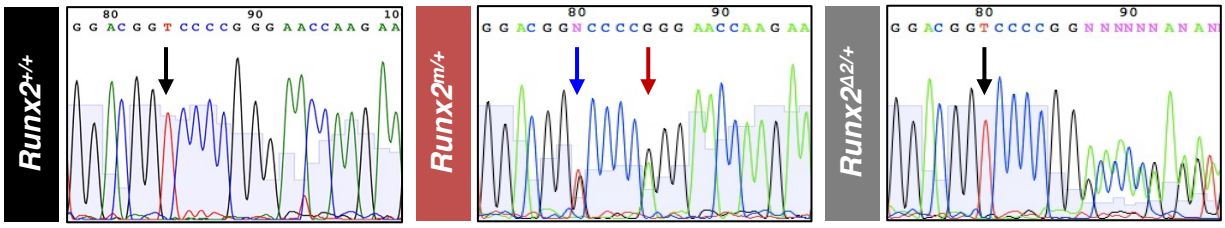

Figure 2

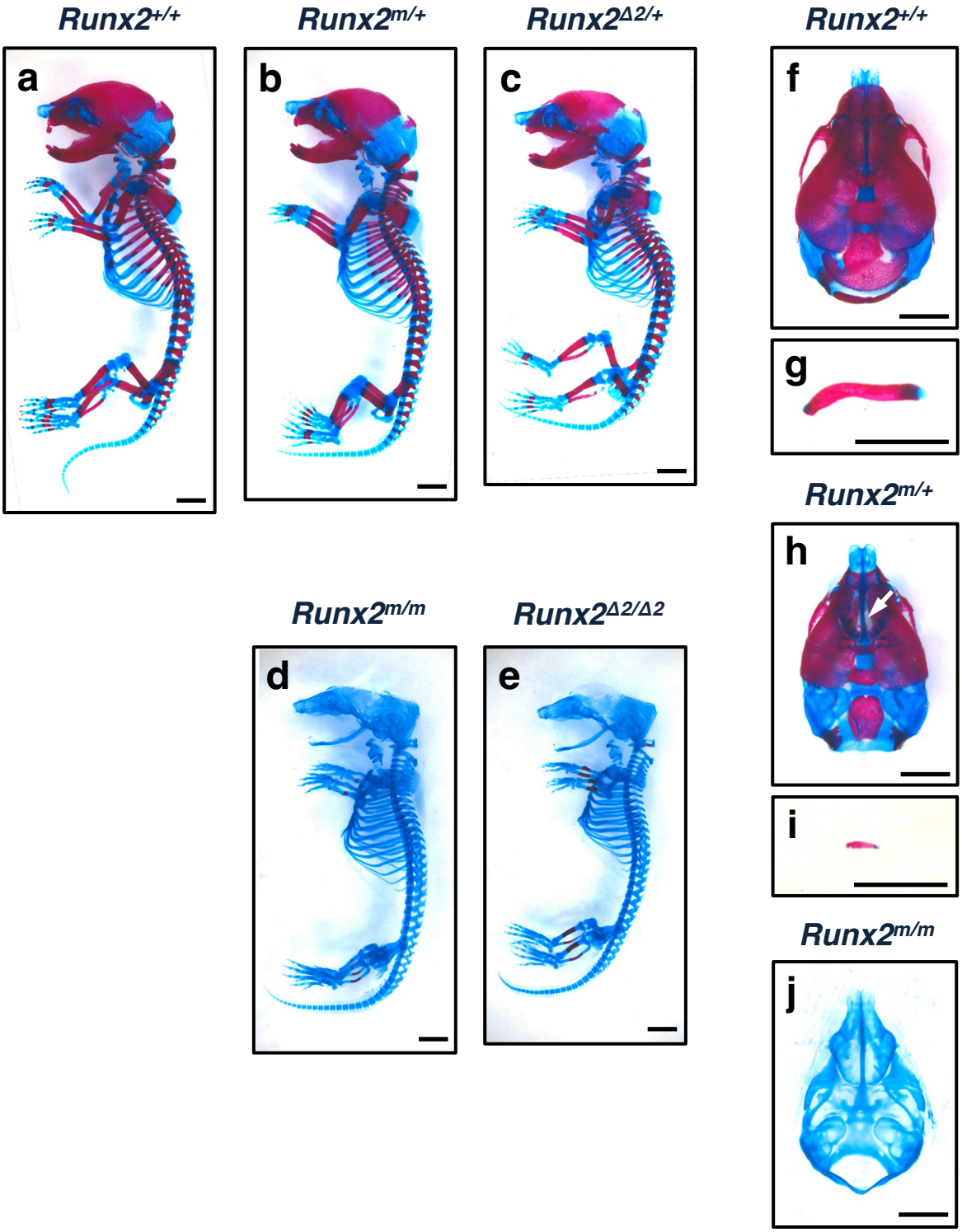
Runx2+/+
a
Runx2m/+
b
Runx2Δ2/+
c
Runx2+/+
f
g
Runx2m/+
h
i
Runx2m/m
d
Runx2Δ2/Δ2
e
Runx2m/m
j

Figure 3

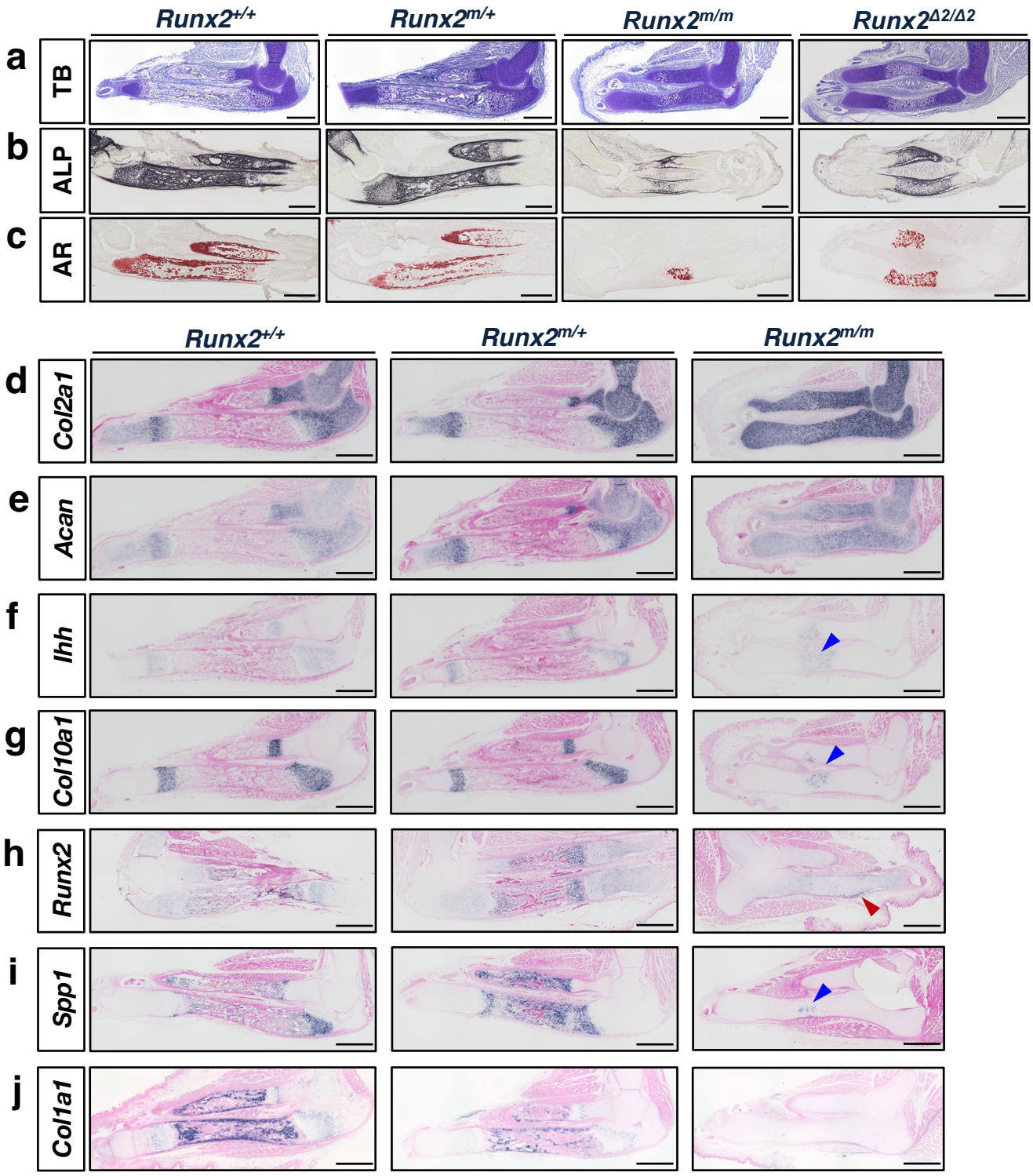
Runx2+/+
Runx2m/+
Runx2m/m
Runx2Δ2/Δ2
a
TB
b
ALP
c
AR
Runx2+/+
Runx2m/+
Runx2m/m
d
Col2a1
e
Acan
f
Ihh
g
Col10a1
h
Runx2
i
Spp1
j
Col1a1

Figure 4

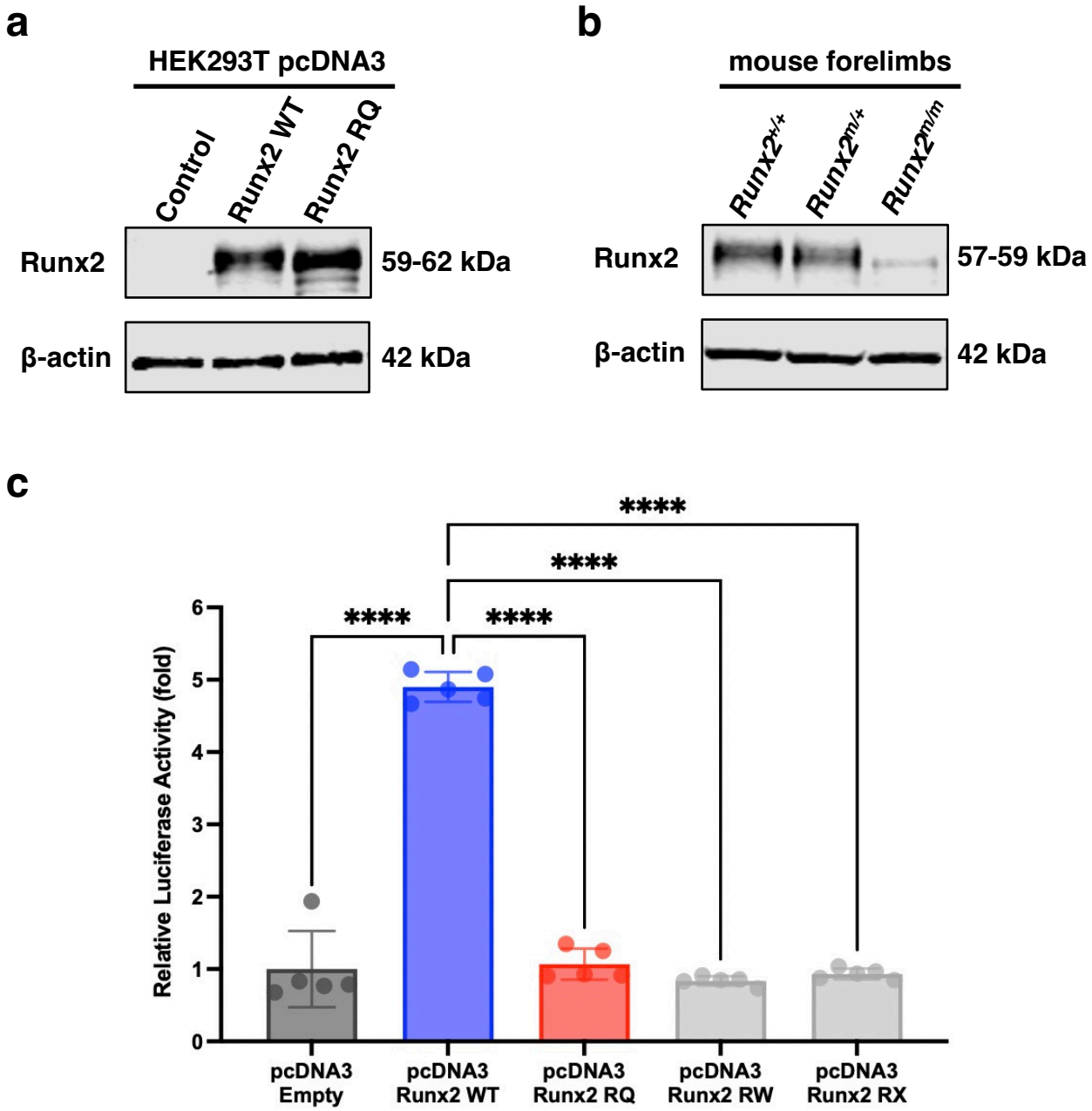
a
HEK293T pcDNA3
Control
Runx2 WT
Runx2 RQ
Runx2
59-62 kDa
β-actin
42 kDa
b
mouse forelimbs
Runx2+/+
Runx2m/+
Runx2m/m
Runx2
57-59 kDa
β-actin
42 kDa
c
****
****
****
****
Relative Luciferase Activity (fold)
0
1
2
3
4
5
6
pcDNA3 Empty
pcDNA3 Runx2 WT
pcDNA3 Runx2 RQ
pcDNA3 Runx2 RW
pcDNA3 Runx2 RX

Figure 5

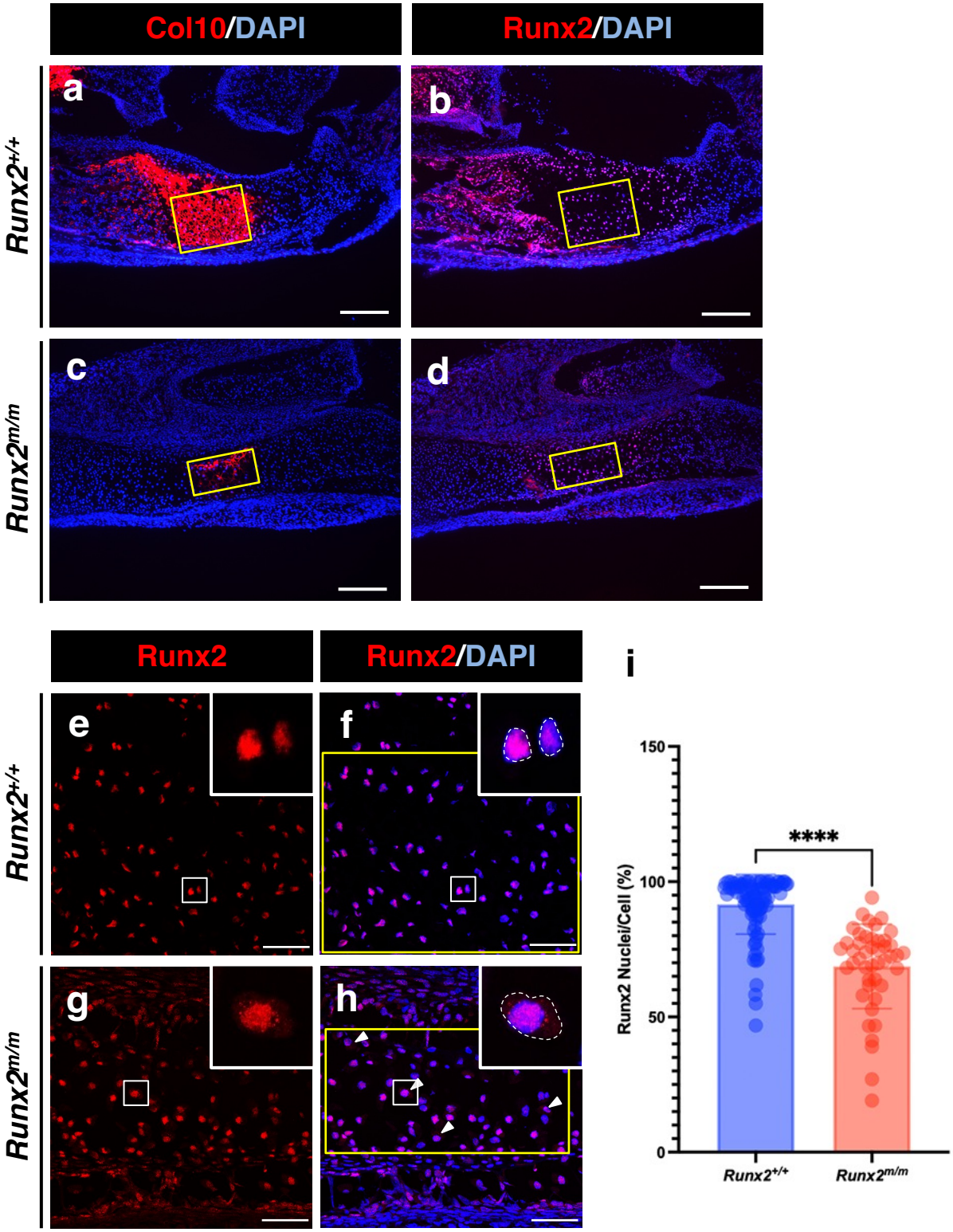
Col10/DAPI
Runx2/DAPI
a
b
c
d
Runx2+/+
Runx2m/m
Runx2
Runx2/DAPI
e
f
g
h
i
Runx2 Nuclei/Cell (%)
150
100
50
0
****
Runx2+/+
Runx2m/m

Figure 6

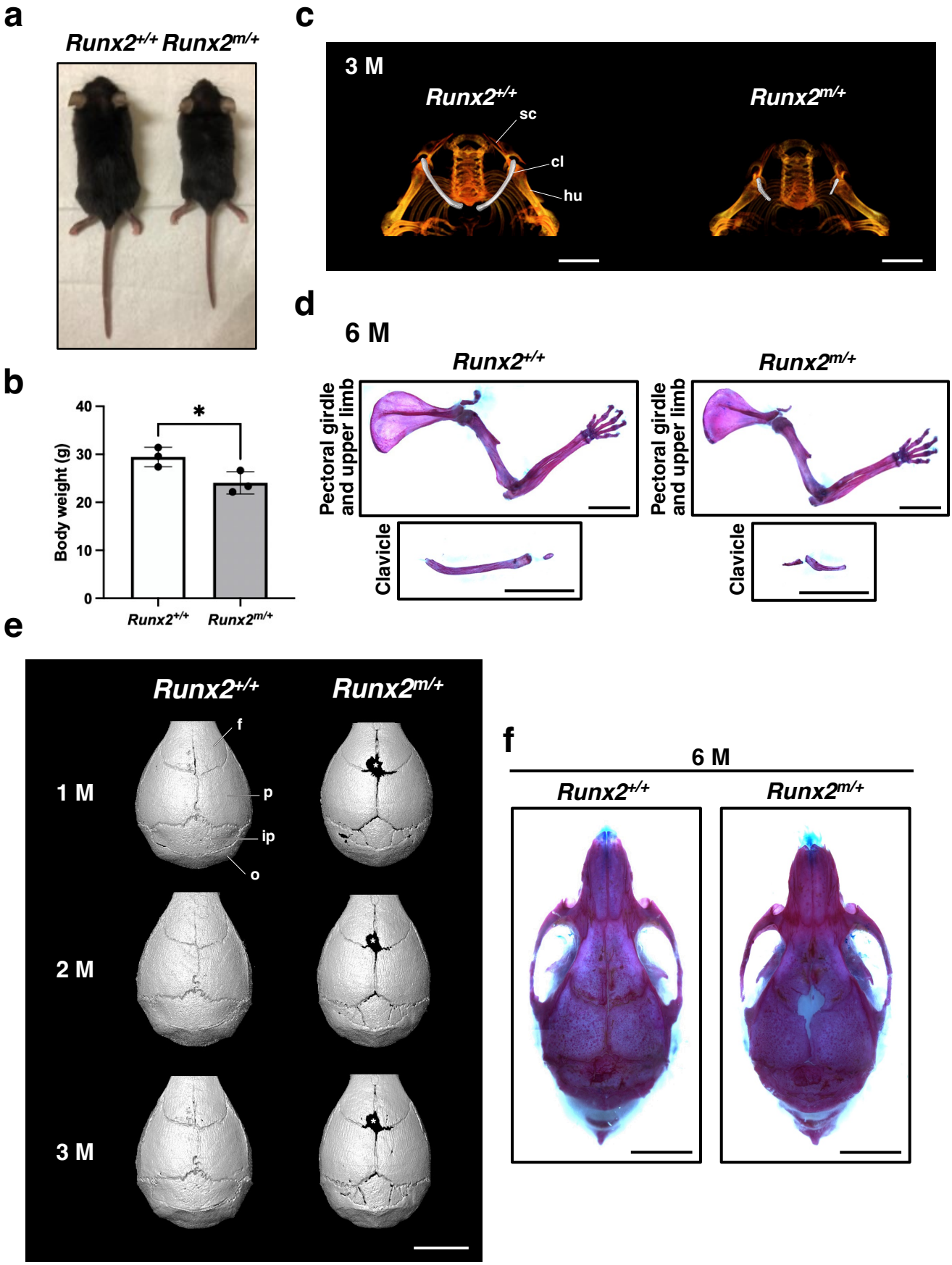
a
Runx2+/+ Runx2m/+
b
Body weight (g)
40
30
20
10
0
*
Runx2+/+
Runx2m/+
c
3 M
Runx2+/+
Runx2m/+
sc
cl
hu
d
6 M
Runx2+/+
Runx2m/+
Pectoral girdle and upper limb
Clavicle
e
Runx2+/+
Runx2m/+
1 M
2 M
3 M
f
f
p
ip
o
6 M
Runx2+/+
Runx2m/+

Figure 7

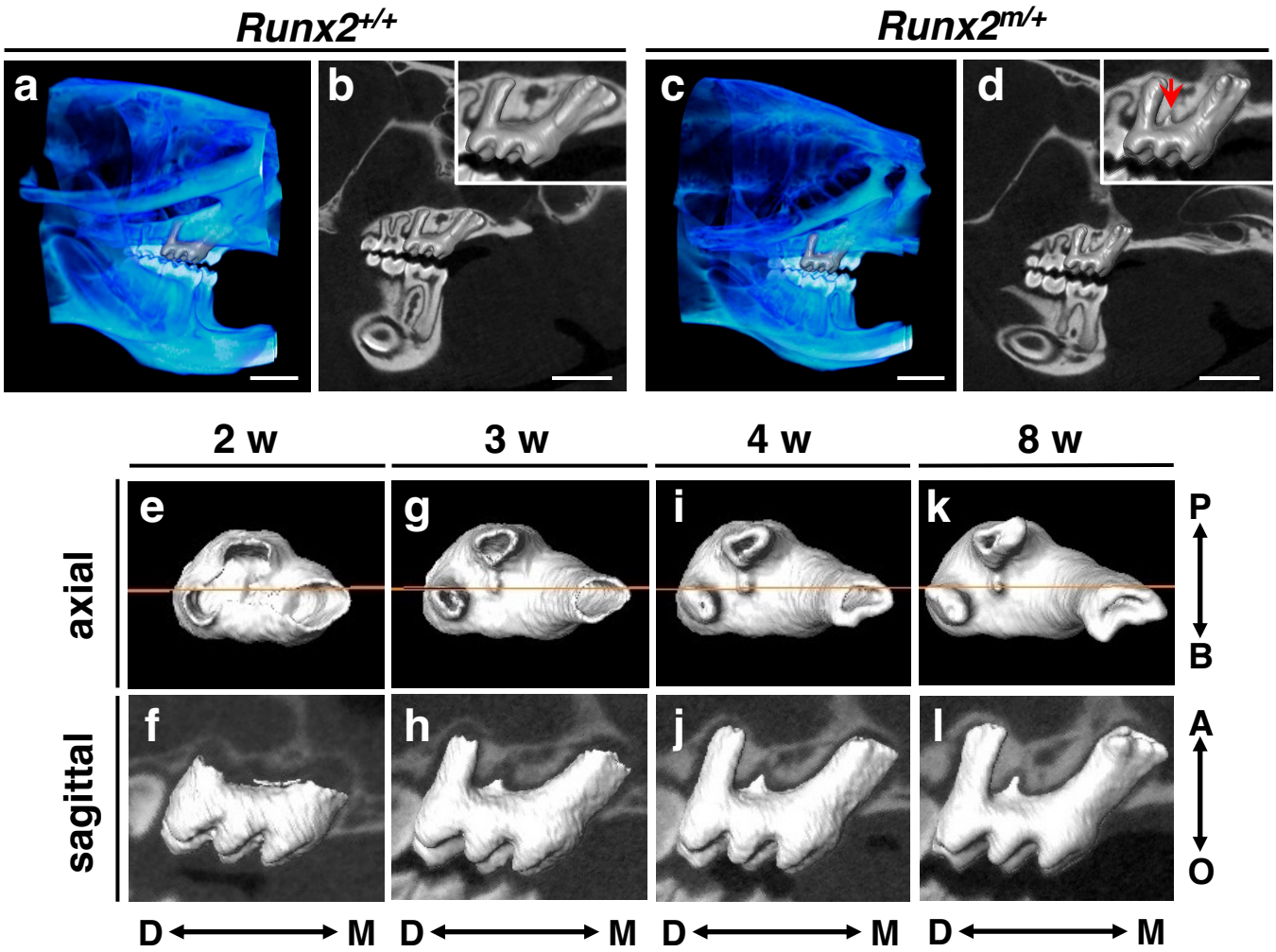
Runx2+/+
Runx2m/+
a
b
c
d
2 w
3 w
4 w
8 w
axial
sagittal
e
g
i
k
f
h
j
l
P
B
A
O
D
M

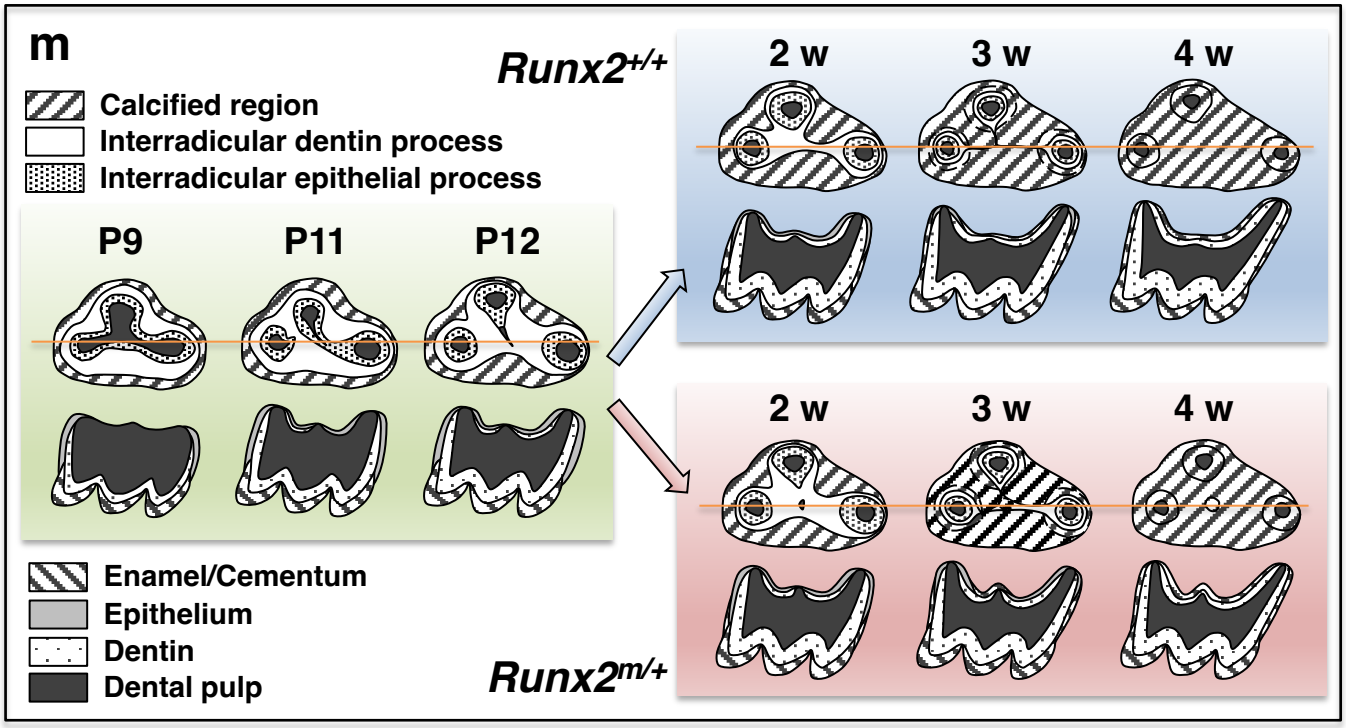
m
Calcified region
Interradicular dentin process
Interradicular epithelial process
P9
P11
P12
Runx2+/+
2 w
3 w
4 w
Runx2m/+
Enamel/Cementum
Epithelium
Dentin
Dental pulp